J. Fluid Mech. (2001), *vol.* 449, *pp.* 141–168. © 2001 Cambridge University Press
DOI: 10.1017/S0022112001006206 Printed in the United Kingdom

Turbulent boundary layer over a compliant surface: absolute and convective instabilities

By K. S. YEO[1], H. Z. ZHAO[2] AND B. C. KHOO[1]

[1]Department of Mechanical Engineering, National University of Singapore, 10 Kent Ridge Crescent, Singapore 119260, Republic of Singapore

[2]Institute of High Performance Computing, 89B Science Park Drive, #01-05/08 The Rutherford, Singapore 118261, Republic of Singapore

(Received 25 April 2000 and in revised form 29 June 2001)

A theoretical model for the instability of two-dimensional turbulent boundary layer over compliant surfaces is described. The principal Reynolds stress is modelled by a well-established mixing-length eddy-viscosity formulation of van Driest. The perturbations of the mean velocity and Reynolds stress fields are coupled via the turbulence model. The investigation of instability is carried out from a time-asymptotic spatio-temporal perspective that classifies instabilities as being either convective or absolute. The occurrence of convective and absolute instabilities over viscoelastic compliant layers is elucidated. Compliant surfaces with low damping are susceptible to convective instability, which gives way to an absolute instability when the surfaces become highly damped. The theoretical results are compared against experimental observations of surface waves on elastic and viscoelastic compliant layers.

1. Introduction

The experiments of Hansen *et al.* (1980), Gad-el-Hak, Blackwelder & Riley (1984) and Gad-el-Hak (1986) show that surface waves on viscoelastic compliant walls under a turbulent boundary layer may be divided into two principal types: the slow waves and the fast waves. The slow waves, whose existence was first noted by Boggs & Hahn (1962), are a series of large-amplitude spanwise-aligned waves that typically propagate at less than 5% of the free-stream speed. They are found on compliant layers possessing a significant level of material damping, and have been termed *static divergence* (SD) waves because of their nearly stationary appearance. The fast waves, on the other hand, are a series of small-amplitude wavetrains that travel with phase speeds in the range of 30–50% of the free-stream velocity. They have only been observed on nearly elastic layers. Gad-el-Hak *et al.* also noted that prior to the occurrence of the SD waves, the mean velocity field and the r.m.s. fluctuations of the turbulent boundary layer on a compliant layer do not differ perceptibly from those on a rigid surface. With the onset of the waves, turbulence in the boundary layer was noticeably enhanced. The latter signifies an altered state of the boundary layer. The occurrence of the slow waves also increases skin-friction drag. These have significant implications for the use of compliant materials in underwater applications.

A good part of what we know about the interaction of flow and compliant boundary has been derived from normal-mode stability analyses of inviscid and laminar boundary-layer flows. At the most basic level, the instabilities may be divided into two groups: flow modes and wall modes. Flow modes refer to modes that are

https://doi.org/10.1017/S0022112001006206 Published online by Cambridge University Press

derivatives of eigenmodes originally present in the same flow over a rigid boundary; the Tollmien–Schlichting (TS) instability of a laminar boundary layer is a prime example. Wall modes pertain to modes that are brought into being by the compliant quality of the wall. They have been termed flow-induced surface instabilities (FISI) by Carpenter & Garrad (1985) and compliance-induced flow instabilities (CIFI) by Yeo (1988). The wall modes are associated with the unstable interaction between the inertia of the flow and the dynamic and static deformation modes of the compliant wall. The former leads to waves that travel at a fair speed (termed *travelling wave flutter* or TWF) whereas the latter produces nearly static waves at incipience (and hence termed a *static divergence* instability). Yeo & Dowling (1987) were able to derive general criteria that relate the occurrence of these waves to the dynamic and static wave-bearing characteristics of a general compliant wall. Benjamin (1960) and Landahl (1962) showed that wall compliance exerts a favourable influence on the TS instability of a laminar boundary layer. Benjamin (1963) introduced a classification of the instabilities based on the energy required to activate or create the waves. The TWF modes are positive-energy waves and are designated Class B by Benjamin. Such waves would be attenuated by wall damping, which removes energy from the dynamical system. The TS waves are negative-energy or Class A waves. They are amplified by wall damping, which removes energy from the system (see Crighton & Oswell 1991). Landahl and Benjamin have also classified the static divergence modes as Class A because they are destabilized by wall damping and appear to require wall damping for their occurrence. Benjamin also introduced a Class C wave. Class C waves, as typified by the Kelvin–Helmholtz instability, are characterized by mainly conservative exchange of wave energy between the flow and the wall. They tend to be relatively insensitive to small variation in wall damping.

The highly distinct surface waves observed in the turbulent-flow experiments of Hansen *et al.* (1980), Gad-el-Hak *et al.* (1984) and Gad-el-Hak (1986) clearly represent deviations from mean-flow conditions that could not be ascribed to random turbulent fluctuations. Indeed, the slow and fast waves exhibit clear semblance with the SD and TWF waves as predicted by temporal stability analysis, and are hence, in all probability, manifestations of wave instability. Duncan, Waxman & Tulin (1985) considered the normal-mode stability of potential flows on compliant layers in which the perturbation fluid pressure was modified by a complex factor $K_p \exp(\mathrm{i}\theta_p)$ to simulate the dynamics of laminar and turbulent boundary layers. Values of K_p and θ_p were obtained from published literature. Despite the relative simplicity of their model, Duncan *et al.*'s results exhibit fairly good qualitative consistency with the experimental results of Gad-el-Hak *et al.* Evrensel & Kalnins (1988) pursued a more traditional line of stability analysis in which the turbulent boundary layer was represented by its time-mean velocity profile. The mean velocity profile was modelled by the $\frac{1}{7}$-power law. They reported some quantitative agreement with the slow-wave results of Gad-el-Hak *et al.* Several other workers, notably Ffowcs Williams (1964), Semenov (1971) and Zimmermann (1974), had also investigated the action of compliant surfaces on turbulent boundary layer by focusing attention on the dynamics of the sublayer, a semi-turbulent regime of the flow adjacent to the wall that governs the production of turbulent vorticity. Although the overall concept underlying their approach appears to be good, progress in this direction has been largely hampered by the lack of a good sublayer model.

The appearance of surface waves on compliant surfaces subject to a turbulent boundary layer is pursued in the present work from the stability viewpoint. The present study differs from those of Duncan *et al.* and Evrensel & Kalnins in two

https://doi.org/10.1017/S0022112001006206 Published online by Cambridge University Press

key areas: the wave growth model and the physical model. Instead of a conventional normal-mode growth model, the time-asymptotic spatio-temporal disturbance growth theory of Briggs (1964) is adopted here. In the realm of physical modelling, the effect of turbulence production is incorporated, whereas the models of both Duncan *et al.* and Evrensel & Kalnins are essentially quasi-laminar.

Briggs' theory shows that an unstable disturbance in an open physical system, such as a boundary layer, evolves in one of two distinctive manners: it may grow in size as it propagates away from its initiating source, in which case it is termed a *convective instability*; or it may grow in an expanding neighbourhood of the source, and is termed an *absolute instability*. Convective instability assumes the appearance of an amplifying travelling wave or wave packet, whereas absolute instability exhibits a stationary appearance because of its non-propagative character, and is moreover self-sustaining when excited. Accounts of the theory may be found in Bers (1983) and Huerre & Monkewitz (1990). The theoretical dichotomy of convective and absolute instabilities matches well the observed behaviour of the fast waves and slow (or SD) waves. Because of the stronger physical basis on which it is founded, the asymptotic spatio-temporal theory offers a more complete picture of the growth and development of instability waves in open dynamical systems than could be gleaned from purely modal analyses. Yeo, Khoo & Zhao (1996) found that absolute instability eigenmodes might exist in a Blasius boundary layer over soft compliant surfaces, although the same flow seems to admit only convective instability on a rigid surface. The theory has also been applied by Yeo, Khoo & Zhao (1999) to modified-potential-flow models of laminar and turbulent boundary layers, following Duncan *et al.* They found, interestingly, that uniform potential flow over compliant surfaces with non-zero damping admits only absolute instability. They also discovered that the onset velocity of convective instability converges rapidly onto the onset velocity of absolute instability for a turbulent boundary layer when the compliant layer possesses significantly high damping, but this is not so for a laminar boundary layer.

Duncan *et al.*'s modified potential flow is clearly inadequate as a mechanistic model for a turbulent boundary layer. Moreover, their model is greatly restricted by its dependence on the availability of suitable data for K_p and θ_p. Evrensel & Kalnins considered a viscous turbulent boundary layer, but their analysis of stability ignored the effects of turbulent stresses. These modelling limitations are remedied in the present study. The present work approaches the stability of the turbulent boundary layer via the unsteady turbulent-averaged momentum equations. The principal turbulent or Reynolds stress is modelled by the well-established mixing-length eddy-viscosity formulation of van Driest (White 1991). The perturbations of the turbulent stress and mean velocity fields are coupled via the turbulence model.

The stability eigenvalue problem for two-dimensional waves in turbulent boundary layers on viscoelastic compliant layers, with Reynolds-stress modelling, is developed in § 2. The governing equations for the flow and wall domains are discretized by a Chebyshev-polynomials collocation procedure, and formulated as a linear matrix eigenvalue problem in the complex frequency ω in § 3; following Yeo *et al.* (1996). Absolute instabilities are associated with the intersection of certain causal pairs of α–eigenvalues (α is the streamwise wavenumber); these are revealed as cusp points by the mapping procedure of Kupfer, Bers & Ram (1987). The occurrence of slow waves and fast waves as absolute and convective instabilities, respectively, is studied in § 5. The instability of spanwise-periodic three-dimensional modes is briefly considered in § 5.9.

https://doi.org/10.1017/S0022112001006206 Published online by Cambridge University Press

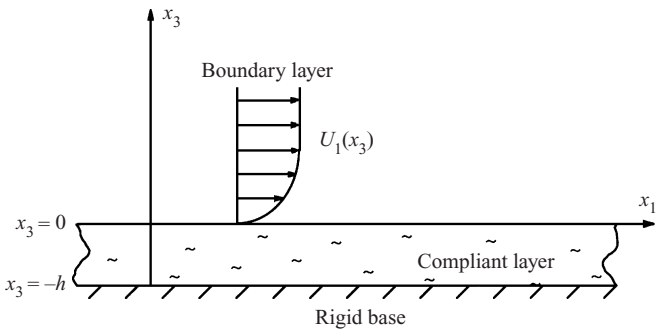


FIGURE 1. Boundary-layer flow over a compliant layer.

2. Theoretical formulation

One of the earliest attempts to apply the concept of stability to turbulent flows was by Markus (1956). Markus postulated that the mean flow field of a turbulent shear flow is determined by the conditions of marginal stability and maximum dissipation. By discarding all nonlinear terms on the assumption that they would be stabilizing, Markus arrived at an Orr–Sommerfeld (OS) stability equation for the mean velocity field. Landahl (1967), on the other hand, retained the nonlinear wave terms and treated them as source terms on the right-hand side of the OS equation to represent the effects of turbulence. The homogeneous OS equation for the turbulent-mean flow was found to contain only decaying modes, of which the lightly damped ones were shown to affect turbulent correlations over large distances. Landahl was interested in how these modes might be driven by the nonlinear effects of turbulence. Both Markus and Landahl did not obtain a closed-form stability problem for the turbulent mean flow, however, because the essential turbulent effects were either omitted or independently specified.

A more systematic attempt at analysing turbulent shear flows from the stability viewpoint was made by Hussain & Reynolds (1970) and Reynolds & Hussain (1972) in the context of a theory for organized waves (coherent structures) in such flows. They introduced the concept of a phase-based ensemble averaging to extract the organized wave information from the flow, and applied an eddy-viscosity model for the oscillatory (perturbation) Reynolds stresses to close the problem. A theory of stability for turbulent layer over compliant surfaces is introduced in the present paper. Turbulent closure is accomplished via mixing-length eddy-viscosity formulation of principal Reynolds stress. The theory differs from that of Reynolds & Hussain in some areas, which will be discussed subsequently.

The physical problem comprises two domains, as shown in figure 1: a semi-bounded incompressible viscous flow region with a zero-pressure-gradient turbulent boundary layer and a viscoelastic compliant layer on a rigid base. The standard Cartesian coordinate frame has its positive x_1-axis pointing in the streamwise direction and x_3-axis pointing vertically upwards. The flow and wall are assumed to be in an initial state of equilibrium in the mean in which the mean flow and the compliant surface spanning the (x_1, x_2)-plane at $x_3 = 0$ are essentially steady (unperturbed) except for small fluctuations associated with the background turbulence of the flow. The mean flow over the surface is identical to that over a rigid surface in this state. The linear stability of the boundary layer, the compliant wall and the interface to small perturbations or changes of their mean fields is considered. Each domain is

https://doi.org/10.1017/S0022112001006206 Published online by Cambridge University Press

governed by its own physical equations. The perturbations in the two domains are kinematically and dynamically coupled along the domain interface at $x_3 = 0$.

2.1. *Stability of two-dimensional turbulent boundary layers*

The dynamics of an unsteady two-dimensional incompressible turbulent viscous fluid is governed by the following turbulence-averaged equations of continuity and momentum:

$$\frac{\partial\langle U_1\rangle}{\partial x_1} + \frac{\partial\langle U_3\rangle}{\partial x_3} = 0, \tag{1}$$

$$\frac{\partial\langle U_1\rangle}{\partial t} + \langle U_1\rangle\frac{\partial\langle U_1\rangle}{\partial x_1} + \langle U_3\rangle\frac{\partial\langle U_1\rangle}{\partial x_3} = -\frac{1}{\rho}\frac{\partial\langle P\rangle}{\partial x_1} + \nu\nabla^2\langle U_1\rangle + \frac{\partial}{\partial x_3}\langle -u_1'u_3'\rangle, \tag{2}$$

$$\frac{\partial\langle U_3\rangle}{\partial t} + \langle U_1\rangle\frac{\partial\langle U_3\rangle}{\partial x_1} + \langle U_3\rangle\frac{\partial\langle U_3\rangle}{\partial x_3} = -\frac{1}{\rho}\frac{\partial\langle P\rangle}{\partial x_3} + \nu\nabla^2\langle U_3\rangle + \frac{\partial}{\partial x_1}\langle -u_1'u_3'\rangle, \tag{3}$$

where $\langle\ \rangle$ denotes a suitable ensemble-averaging operation. $\langle U_1, U_3\rangle$ and $\langle P\rangle$ represent the ensemble-averaged velocity and pressure fields, respectively. Only the dominant component $\langle -u_1'u_3'\rangle$ of the Reynolds (turbulent) stress tensor has been retained in equations (2) and (3).

The Reynolds stress tensor represents the total effects that turbulent fluctuations have on the mean fields, for its presence distinguishes equations (2) and (3) from the Navier–Stokes equations. The small-scale stochastic motions of turbulence are the principal contributor to the production of turbulent shear stress in a wall shear layer (Hinze 1975). The large-scale motions play an essential role in maintaining the self-perpetuating cycles of turbulence, but only affect turbulent shear stress production in an indirect manner. Equations (2) and (3) may thus be applied to events of the turbulent-mean fields whose spatial and temporal scales are considerably larger than the scales of turbulent motions that directly contribute to the Reynolds stress terms. Indeed, the bulk of turbulence production in a turbulent boundary layer is concentrated in a thin wall layer characterized by the inner length scale of ν/u_* and timescale of ν/u_*^2 (Tennekes & Lumley 1972); where ν and u_* are the kinematic viscosity of the fluid and the wall-friction velocity, respectively. These are significantly smaller than the length scales and time scales of the unstable dynamical events that we seek to study here, which are typically of the order of the gross boundary-layer thickness δ and time scale δ/U_∞, respectively, or larger. For a turbulent boundary layer based on the $\frac{1}{7}$-power law, these characteristic turbulence scales are $O(R_\delta^{-11/12})$ and $O(R_\delta^{-5/6})$ relative to the length and time scales of the boundary layer, where $R_\delta = \delta U_\infty/\nu$ is the Reynolds number based on the boundary-layer thickness.

$\langle\ \rangle$ may be the phase-based ensemble-average of Hussain & Reynolds (1970); since the emergence of a sinusoidal wave would be immediately recognizable as the growth of an organized wave structure. A time-based average may also be applicable if equations (2) and (3) are intended to model or detect the onset of events that lead to a permanent or large time-scale departure of the flow from its original state. In this case, the averaging period would, of course, have to be significantly longer than the time scales of the random turbulent fluctuations that we wish to ignore. Experimental evidence indicates that the onset of SD waves affects both the turbulence and mean characteristics of the base flow.

The van Driest mixing-length eddy-viscosity approximation of $\langle -u_1'u_3'\rangle$ (see White 1991) is used to close the above equations. The model is well established and produces results that accurately match experimental measurements for the flat-plate boundary

https://doi.org/10.1017/S0022112001006206 Published online by Cambridge University Press

layer. This suggests that the model adequately represents the physics of this relatively simple turbulent flow. The model has also been employed extensively in the numerical computation of non-separating two-dimensional turbulent boundary layers (Cebeci & Bradshaw 1977). The more complex turbulent models available in the literature (Speziale 1991) are generally intended to deal with a larger class of fluid flows. They are not assured to give better results for the present relatively simple flow. Accordingly, we have

$$\langle -u_1' u_3' \rangle = \nu_t \left(\frac{\partial \langle U_1 \rangle}{\partial x_3} + \frac{\partial \langle U_3 \rangle}{\partial x_1} \right), \tag{4a}$$

where

$$\nu_t = l^2 \frac{\partial \langle U_1 \rangle}{\partial x_3}, \tag{4b}$$

is the eddy-viscosity coefficient. The absolute value function has been ignored because $\partial \langle U_1 \rangle / \partial x_3 \geqslant 0$ for the flows considered in this paper. The mixing length l is prescribed by the composite van Driest law:

$$l(x_3) = \begin{cases} kx_3 \left[1 - \exp\left(-\dfrac{x_3}{A} \right) \right] & \text{for} \quad x_3 \leqslant x_3^c, \\ 0.09\delta & \text{for} \quad x_3 > x_3^c, \end{cases} \tag{5}$$

where δ is the boundary-layer thickness. The von Kármán constant k and the damping-length constant A are assigned their empirically established values of 0.41 and $26(\nu/u_*)$, respectively. The term x_3^c denotes the point at which the two expressions for $l(x_3)$ have equal value.

Let (U_1, U_3), P and $-\overline{u_1' u_3'}$ denote the mean velocity, pressure and Reynolds stress fields of a steady turbulent boundary layer over a compliant layer. To investigate the stability of the steady mean fields, we subject the mean fields to a small variation (perturbation):

$$\langle U_1 \rangle = U_1 + u_1, \quad \langle U_3 \rangle = U_3 + u_3, \quad \langle P \rangle = P + p, \quad \langle -u_1' u_3' \rangle = -\overline{u_1' u_3'} + \tau,$$

where (u_1, u_3), p and τ denote the small perturbations or changes made to the mean velocity, pressure and turbulent stress fields, respectively. We then seek to discover how the altered mean fields will evolve in terms of the growth or decay of the applied perturbation.

The perturbed fields are governed by equations (1) and (3). Substituting these into the governing equations, eliminating the initial steady mean state and retaining only terms that are first-order in the perturbation quantities yield a system of linear partial differential equations in the perturbation quantities. By further invoking the locally parallel-flow approximation for a leading-order stability analysis, we obtain the following system of equations for the perturbation field quantities (u_1, u_3), p and τ:

$$\frac{\partial u_1}{\partial x_1} + \frac{\partial u_3}{\partial x_3} = 0, \tag{6}$$

$$\frac{\partial u_1}{\partial t} + U_1 \frac{\partial u_1}{\partial x_1} + u_3 \frac{\partial U_1}{\partial x_3} = -\frac{1}{\rho} \frac{\partial p}{\partial x_1} + \nu \nabla^2 u_1 + \frac{\partial \tau}{\partial x_3}, \tag{7}$$

$$\frac{\partial u_3}{\partial t} + U_1 \frac{\partial u_3}{\partial x_1} = -\frac{1}{\rho} \frac{\partial p}{\partial x_3} + \nu \nabla^2 u_3 + \frac{\partial \tau}{\partial x_1}. \tag{8}$$

Only the U_1 component of the mean velocity field and its x_3-derivative are involved

https://doi.org/10.1017/S0022112001006206 Published online by Cambridge University Press

above. With the same linear and parallel-flow approximations, the perturbation component of turbulent stress τ may be derived from (4) to be

$$\tau = l^2 \frac{\partial U_1}{\partial x_3}\left(2\frac{\partial u_1}{\partial x_3} + \frac{\partial u_3}{\partial x_1}\right). \tag{9}$$

Equations (6)–(9) constitute a complete system of four equations for the four perturbation quantities u_1, u_3, p and τ when the x_1-velocity field U_1 of the steady turbulent-mean flow is prescribed. Depending on whether the perturbation fields die away or amplify with time, we say the original mean fields are stable or unstable, respectively.

The governing equations (6)–(9) for the perturbation fields can be further simplified by introducing the perturbation stream function Ψ and assuming the perturbation to have the form of a sinusoidal travelling wave:

$$u_1 = \frac{\partial \Psi}{\partial x_3}, \quad u_3 = -\frac{\partial \Psi}{\partial x_1}, \tag{10a,b}$$

$$\Psi(x_1, x_3, t) = \psi(x_3)\exp[\mathrm{i}(\alpha x_1 - \omega t)], \tag{11}$$

where α and ω are the wavenumber and frequency of the wave, respectively. The substitution of these into equations (6)–(9) and the elimination of the pressure terms then result in the following equation:

$$(U_1 - c)(\psi'' - \alpha^2\psi) - U_1''\psi = -\frac{1}{\mathrm{i}\alpha R_{\delta^*}}(\psi^{(4)} - 2\alpha^2\psi'' + \alpha^4\psi) + \frac{\chi}{\mathrm{i}\alpha}\sum_{j=0}^{4} F_j \psi^{(j)}, \tag{12}$$

where $c = \omega/\alpha$ is the phase speed of the perturbation wave. The prime is used here and below to indicate an ordinary derivative with respect to x_3. The coefficients F_j are given by:

$$F_0 = \alpha^2 U_1''' l^2 + 4\alpha^2 U_1'' l l' + 2\alpha^2 U_1' l l'' + 2\alpha^2 U_1' l' l' + \alpha^4 U_1' l^2, \tag{13a}$$

$$F_1 = 2\alpha^2 U_1'' l^2 + 4\alpha^2 U_1' l l', \quad F_2 = 2U_1''' l^2 + 8U_1'' l l' + 4U_1' l l'' + 4U_1' l' l' + 3\alpha^2 U_1' l^2, \tag{13b,c}$$

$$F_3 = 4U_1'' l^2 + 8U_1' l l', \quad F_4 = 2U_1' l^2. \tag{13d,e}$$

The quantities of equation (12) have all been non-dimensionalized with respect to the free-stream velocity U_∞, fluid density ρ and displacement thickness δ^* of the boundary layer. $R_{\delta^*} = U_\infty \delta^*/\nu$ denotes the Reynolds number based on displacement thickness. The term χ is an artificial intermittency factor that is inserted to allow the theory to be applied in the transitional region between the laminar and fully turbulent parts of the boundary-layer flow. When the intermittency factor χ is set to zero, we have the case of a laminar flow, and equation (12) then reduces to the well-known Orr–Sommerfeld equation. The value of χ is set to 1.0 throughout this study. Equation (12) is termed the turbulent Orr–Sommerfeld equation here for ease of reference.

The perturbation of the mean flow induces fluctuations of the fluid stresses

$$\sigma_{13}^{(f)} = \hat{\sigma}_{13}^{(f)}(x_3)\exp[\mathrm{i}(\alpha x_1 - \omega t)], \quad \sigma_{33}^{(f)} = \hat{\sigma}_{33}^{(f)}(x_3)\exp[\mathrm{i}(\alpha x_1 - \omega t)], \tag{14a,b}$$

whose x_3-dependent amplitude functions are given by

$$\hat{\sigma}_{13}^{(f)} = \frac{1}{R_{\delta^*}}\left(\psi'' + \alpha^2\psi + \frac{1}{c}U''\psi\right) + \hat{\tau}, \tag{15a}$$

$$\hat{\sigma}_{33}^{(f)} = \frac{\mathrm{i}}{\alpha R_{\delta^*}}\psi''' - \left(c + \frac{3\mathrm{i}\alpha}{R_\delta}\right)\psi' + U_1\psi' - U_1'\psi - \frac{\hat{\tau}'}{\mathrm{i}\alpha}, \tag{15b}$$

https://doi.org/10.1017/S0022112001006206 Published online by Cambridge University Press

where

$$\hat{\tau} = \chi U_1' l^2 (2\psi'' + \alpha^2 \psi), \quad \hat{\tau}' = \chi \sum_{j=0}^{3} G_j \psi^{(j)}, \tag{16a,b}$$

and

$$G_0 = \alpha^2 (U_1'' l^2 + 2U_1' l l'), \quad G_1 = \alpha^2 U_1' l^2, \tag{17a,b}$$

$$G_2 = 2U_1'' l^2 + 4U_1' l l', \quad G_3 = 2U_1' l^2. \tag{17c,d}$$

The $\sigma_{11}^{(f)}$ component of fluctuating fluid stress is not listed because it is not required in the subsequent development.

Reynolds & Hussain (1972) showed that the oscillation of the Reynolds stress, $\tilde{r}_{ij} = \langle -u_i' u_j' \rangle - (-\overline{u_i' u_j'})$, induced by an organized-wave perturbation of the turbulent mean flow is of the same order of magnitude as the organized wave $O(u)$ itself. The same may also be observed in equation (9) of the present theory. They then closed the stability problem by adopting an eddy-viscosity model for the oscillatory Reynolds stress:

$$\tilde{r}_{ij} = \nu_t \left(\frac{\partial u_i}{\partial x_j} + \frac{\partial u_j}{\partial x_i} \right), \tag{18}$$

in which the eddy-viscosity coefficient ν_t was taken to be either a constant or prescribed by a van Driest type model. Sen & Veeravalli (1998) took the development of Reynolds & Hussain one step further by applying an anisotropic Reynolds-stress model of Pope (1975) for the $\tilde{r}_{ij}$. They found that the turbulent mean flow supports unstable eigenmodes if a certain anisotropy function possesses large values in the vicinity of the wall.

The present formulation differs from the theory of Reynolds & Hussain in one key aspect. Whereas they had invoked turbulent closure at the level of the perturbation Reynolds stress $\tilde{r}_{ij}$, we have applied the same to the Reynolds stress $\langle -u_1' u_3' \rangle$ at the level of the full momentum equations (2)–(3). The fluctuation or perturbation of the Reynolds stress in our case then arises from the fluctuation of the mean velocity field via the turbulence model for the Reynolds stress $\langle -u_1' u_3' \rangle$. The eddy-viscosity coefficient ν_t was taken to be at most a prescribed function of x_3 in Reynolds & Hussain. In our case, the ν_t also fluctuates in sympathy with the perturbation of the turbulent mean field in accordance with the adopted mixing-length mechanism (4*b*). This results in an anisotropic perturbation Reynolds stress (9), which has a factor of 2 for $\partial u_1 / \partial x_3$, in contrast to the isotropic model of Reynolds & Hussain (equation (18)). The ν_t is also a function of x_3 in Sen & Veeravalli, although other anisotropic terms are added to (18). In the present formulation, the turbulent mean flow and modelled Reynolds stress field $\langle -u_1' u_3' \rangle$ are coupled by the conservation of mean momentum via equations (2) and (3); any changes (perturbation) of the mean fields are necessarily matched by corresponding changes (perturbation) of the Reynolds stress field in a manner that is consistent with the adopted turbulence model. In Hou (1996), a precursor of the present work, the steady turbulent mean velocity field U_1 was in fact also computed directly from the turbulence model by integrating a boundary-layer version of the full momentum equations.

2.2. *Turbulent mean flow*

The steady turbulent-averaged or mean velocity profile of the fluid boundary layer is governed by the choice of the turbulent stress model. The mean velocity distribution U_1

https://doi.org/10.1017/S0022112001006206 Published online by Cambridge University Press

for the inner region of the boundary layer is given here by the integration of the van Driest law of the wall (equation (5)). Extension to the outer or turbulent wake region is accomplished by the addition of a wake function. The velocity distribution thus has the form of:

$$\frac{U_1(x_3)}{u_*} = u_1^+ = \int_0^{x_3^+} + \frac{2}{1+\sqrt{1+4k^2(x_3^+)^2[1-\exp(-x_3^+/A^+)]^2}}\mathrm{d}x_3^+ + \frac{\Pi}{k}W\left(\frac{x_3}{\delta}\right), \tag{19}$$

where u_1^+ and $x_3^+ = x_3 u_*/\nu$ are the inner-wall variables. The friction velocity $u_* = U_\infty\sqrt{c_f/2}$ is calculated from the local friction coefficient c_f. For the flat-plate turbulent boundary layer

$$c_f = \frac{0.455}{\ln^2(0.06R_x)}, \tag{20}$$

where $R_x = U_\infty x_1/\nu$ is the x_1-Reynolds number. The term R_x is related to the displacement-thickness Reynolds number R_{δ^*} by the relation $R_{\delta^*} \cong 0.018(R_x)^{6/7}$. For a value of $A^+ = 26$, the integral in (19) accurately defines the velocity distribution in the entire inner region of the boundary layer, comprising the sublayer, the buffer and the overlap regions (White 1991). The wake parameter Π in (19) is in general a function of x_1. For flow with zero pressure gradient, Π is a constant equal to about 0.55 (Coles 1956). The wake function $W(x_3/\delta)$ is given to a good approximation by the following empirical fit:

$$W\left(\frac{x_3}{\delta}\right) = 2\sin^2\frac{\pi}{2}\left(\frac{x_3}{\delta}\right), \tag{21}$$

where δ is the thickness of the boundary layer. The approximate relation $\delta = 7.78\delta^*$ is employed here to calculate δ when the displacement-thickness Reynolds number R_{δ^*} is specified. Equation (19) defines a continuous velocity distribution U_1 over the whole boundary layer that is in very good agreement with experimental measurements. The derivatives of U_1 are obtained from U_1 by numerical differentiation and interpolation. The velocity distribution may alternatively be obtained by directly integrating the steady turbulent boundary-layer equations.

2.3. *Wave dynamics of a compliant wall*

The compliant wall is represented here by a layer of homogeneous isotropic viscoelastic material of uniform thickness. Associated with the harmonic wave perturbation of the flow (equation (11)) is a corresponding two-dimensional travelling-wave perturbation of the compliant layer. The displacement vector field (η_1, η_3) of the wall perturbation thus has the form of:

$$(\eta_1, \eta_3) = (\hat{\eta}_1, \hat{\eta}_3)\exp[\mathrm{i}(\alpha x_1 - \omega t)], \tag{22}$$

where $\hat{\eta}_1$ and $\hat{\eta}_3$ are the x_3-dependent amplitude functions.

Harmonic wave propagation in a homogeneous isotropic viscoelastic material, with zero body force, is governed by the following viscoelastic analogue of Navier's equation:

$$G(\hat{\eta}_1'' - \alpha^2\hat{\eta}_1) - (K + G/3)(\alpha^2\hat{\eta}_1 - \mathrm{i}\alpha\hat{\eta}_3') + \rho\omega^2\hat{\eta}_1 = 0, \tag{23a}$$

$$G(\hat{\eta}_3'' - \alpha^2\hat{\eta}_3) - (K + G/3)(\hat{\eta}_3'' + \mathrm{i}\alpha\hat{\eta}_1') + \rho\omega^2\hat{\eta}_3 = 0, \tag{23b}$$

where G and K are the shear and bulk moduli of the material, respectively. Viscoelastic

https://doi.org/10.1017/S0022112001006206 Published online by Cambridge University Press

material damping is modelled by a Kelvin–Voigt model for the shear modulus G. For harmonic time variation, G may be written in the complex form of $G = \rho C_t^2 - \mathrm{i}\omega d$, where C_t and d are the elastic shear wave speed and damping coefficient of the material, respectively. The bulk modulus K has been assumed to be real, for simplicity, so that there is no damping in dilatational deformation. This assumption is good for nearly incompressible materials, which is the class of materials studied in this work. The fluctuating components of the stress tensor in the wall are given by

$$\sigma_{13}^{(w)} = \hat{\sigma}_{13}^{(w)}(x_3)\exp[\mathrm{i}(\alpha x_1 - \omega t)], \quad \sigma_{33}^{(w)} = \hat{\sigma}_{33}^{(w)}(x_3)\exp[\mathrm{i}(\alpha x_1 - \omega t)], \tag{24a,b}$$

where

$$\hat{\sigma}_{13}^{(w)} = G(\hat{\eta}_1' + \mathrm{i}\alpha\hat{\eta}_3), \quad \hat{\sigma}_{33}^{(w)} = 2G\hat{\eta}_3' + (K + \tfrac{1}{3}G)(\mathrm{i}\alpha\hat{\eta}_1 + \hat{\eta}_3'). \tag{25a,b}$$

2.4. *Fluid–wall interaction and the eigenvalue problem*

The dynamical interaction of flow and the compliant wall is governed by the continuity of velocity and traction at the interface, in its displaced position. These are linearized by Taylor's expansion to apply at the mean interface at $x_3 = 0$:
(i) the continuity of velocity,

$$\psi' = -U_1'\hat{\eta}_3 - \mathrm{i}\omega\hat{\eta}_1, \quad \psi = \frac{\omega}{\alpha}\hat{\eta}_3, \tag{26a,b}$$

(ii) the continuity of traction,

$$\hat{\sigma}_{13}^{(f)} = \hat{\sigma}_{13}^{(w)}, \quad \hat{\sigma}_{33}^{(f)} = \hat{\sigma}_{33}^{(w)}, \tag{27a,b}$$

where $\hat{\sigma}_{13}^{(f)}$, $\hat{\sigma}_{33}^{(f)}$, $\hat{\sigma}_{13}^{(w)}$ and $\hat{\sigma}_{33}^{(w)}$ are the stresses of the flow and compliant wall, as given by (15) and (25), duly evaluated at $x_3 = 0$. The perturbation stream function ψ and the wall displacement vector (η_1, η_3) are also subject to the following conditions:

$$\psi \to 0, \quad \psi' \to 0 \qquad \text{as} \quad x_3 \to \infty, \tag{28}$$

which signifies that the flow perturbation vanishes to zero in the far field; and

$$\hat{\eta}_1(-h) = \hat{\eta}_3(-h) = 0, \tag{29}$$

for the perfect adhesion of the compliant layer, at its lower face at $x_3 = -h$, to the rigid base.

The governing equations for flow perturbation (equation (12)) and wall perturbation (equation (23)), the interface conditions (equations (26) and (27)) and the boundary conditions (equations (28) and (29)) form a closed system of homogeneous equations that constitutes a stability eigenvalue problem

$$D(\alpha, \omega, R_{\delta^*}) = 0. \tag{30}$$

The dependence on wall parameters in (30) has been suppressed for notational brevity.

3. Numerical implementation

The stability problem is transformed into a linear matrix eigenvalue problem in the complex frequency ω by a collocation procedure, whereby the perturbation eigenfunctions of the flow ψ and wall $(\hat{\eta}_1, \hat{\eta}_3)$ are approximated by Chebyshev polynomial series of Nth and Mth order, respectively:

$$\psi(x_3) = \sum_{j=0}^{M} a_j T_j[\xi(x_3)], \tag{31}$$

https://doi.org/10.1017/S0022112001006206 Published online by Cambridge University Press

$$\hat{\eta}_1(x_3) = \sum_{j=0}^{N} b_j T_j[\zeta(x_3)], \quad \hat{\eta}_3(x_3) = \sum_{j=0}^{N} c_j T_j[\zeta(x_3)], \tag{32a,b}$$

with complex coefficients a_j, b_j and c_j. $\xi(x_3)$ and $\zeta(x_3)$ are the transformation functions:

$$\xi = \frac{x_3 - 1}{x_3 + 1}, \quad \zeta = \frac{2x_3}{h} + 1, \tag{33}$$

that map the semi-infinite fluid domain $[0, \infty)$ and the wall domain $[-h, 0]$, respectively, onto the domain of definition $[-1, 1]$ of the Chebyshev polynomials.

The substitution of (31) and (32) into the corresponding governing equations, interface conditions and boundary conditions, and their evaluation at the collocation points then yield a matrix eigenvalue equation of the form:

$$[\boldsymbol{A} - \omega \boldsymbol{B}](\boldsymbol{a}, \boldsymbol{b}, \boldsymbol{c}, \omega \boldsymbol{b}, \omega \boldsymbol{c})^T = \boldsymbol{0}, \tag{34}$$

where $\boldsymbol{a} = (a_0, a_1, \ldots, a_M)$, $\boldsymbol{b} = (b_0, b_1, \ldots, b_N)$ and $\boldsymbol{c} = (c_0, c_1, \ldots, c_N)$. The $\omega \boldsymbol{b}$ and $\omega \boldsymbol{c}$ are auxiliary vectors introduced to linearize the quadratic occurrences of the complex frequency ω in the wall equations. $\mathrm{Det}[\boldsymbol{A} - \omega \boldsymbol{B}] = 0$ yields a numerical equivalent of the dispersion relation (30). For prescribed Reynolds number R_δ, wavenumber δ and wall properties, all the temporal eigenvalues ω of (34) may be obtained using the QZ algorithm. Unlike traditional shooting methods, no guess values are required. The numbers M and N are typically 50–60 and 15–20, respectively. These numbers are frequently checked and increased if necessary to ensure adequate convergence of the eigenvalues.

4. Absolute and convective instabilities

The initial-value space–time response of an open system subjected to a point perturbation at $x_1 = 0$ is described by the Green's function:

$$G(x_1, t) = \int_L \frac{\mathrm{d}\omega}{2\pi} I(x_1, \omega) \exp(-\mathrm{i}\omega t), \tag{35}$$

where

$$I(x_1, \omega) = \int_F \frac{\mathrm{d}\alpha}{2\pi} D^{-1}(\alpha, \omega) \exp(\mathrm{i}\alpha x_1), \tag{36}$$

and $D(\alpha, \omega)$ denotes the dispersion function in (30). The contour F of the Fourier integral is defined along the real axis of the α-plane, while the Laplace contour L is placed above all the singularities of the integral $I(x_1, \omega)$ in the upper ω-plane to satisfy the causal requirement that there is null response prior to an initial time $t = 0$.

The existence of instability, which affects the long-term or asymptotic-time behaviour of the system, is abstracted by deforming the contour L in a continuous manner onto the real ω-axis whilst maintaining the analyticity of the response function. An absolute instability mode is revealed if this process is prevented by the occurrence of a branch-pole singularity in $I(x_1, \omega)$; the latter is caused by the coalescence of two or more α-eigenvalues (α-roots of the dispersion relation) that had originated from different sides (upstream and downstream sides of source) of the Fourier contour F. The perturbation associated with an absolute instability grows in an expanding neighbourhood of the initiating source, and is moreover self-sustaining when excited. It also has zero group velocity, so that an incipient absolute instability exhibits a stationary or non-travelling appearance.

https://doi.org/10.1017/S0022112001006206 Published online by Cambridge University Press

If there is no absolute instability, the system may still be convectively unstable if one or more parts of the contour F have to be deformed off the real α-axis to preserve the analyticity of $I(x_1, \omega)$ when the contour L is fully accommodated along the real ω-axis. An unstable convective mode grows in size as it propagates away from the initiating source. At any given spatial point, the perturbation dies away with time unless otherwise maintained by the source. From the above, it is clear that absolute instability is a highly devastating form of instability, whose growth would be eventually equilibrated by nonlinear effects, whereas a convective instability is largely a driven mode. A fuller account of the theory is given by Bers (1983).

The eigenmodes of absolute and convective instabilities may be found from a careful analysis of the dispersion relation (equation (30)), though the process is usually highly laborious. This task is made more difficult when the dispersion relation is not explicitly given, but is only implicitly defined by a set of differential equations and boundary conditions, as in the present problem. A mapping procedure devised by Kupfer *et al.* (1987) is used in the present study to locate the branch-point singularities associated with absolute instability. The method exploits the period-doubling characteristics of the $\alpha \mapsto \omega$ dispersion map in the vicinity of the intersection point α_0 of two α-roots. The map transforms a smooth contour passing through α_0 in the α-plane into a contour in the ω-plane with a cusp at the image point ω_0. When $(\omega_0)_i > 0$, a possible absolute instability mode is indicated. The causality of a mode is checked by drawing a straight ray from the cusp point ω_0 vertically upwards and observing the number of times this ray intersects the image contour of the α_r-axis ($\alpha_i = 0$) in the ω-plane. An odd number of intersections indicates a causal mode. Convective instabilities, on the other hand, are given by causal spatially growing (upstream or downstream) eigenmodes for real eigenfrequencies. For the downstream modes in particular, these are the eigenstates with $\alpha_i < 0$ lying along the real axis of the ω-plane. The causality of these modes may be checked by the same vertical-ray criterion.

5. Results and discussion

5.1. *Temporal eigenvalue spectra of rigid and compliant surfaces*

The matrix eigenvalue problem (equation (34)) for a zero-pressure-gradient turbulent boundary layer on a rigid surface was solved for an extensive range of wavenumber α and Reynolds number R_{δ^*}. The temporal spectra were found to comprise only damped modes. This is not unexpected, as similar observations had been made by Landahl (1967), Markus (1956) and others. (More recently, Sen & Veeravalli (1998) reported the presence of unstable eigenmodes when they applied a perturbation Reynolds-stress model with strong anisotropy at the rigid wall. What this may imply for the equilibrium state of the turbulent boundary layer is unclear.) The four least-damped discrete eigenmodes for α ranging from 0.1 to 0.9 and $R_{\delta^*} = 1000$ are depicted in figure 2. The two least-damped modes for $\alpha = 0.1$, 0.5, 0.9 and $R_{\delta^*} = 1000$, 3000 are also given in table 1. In all the above cases, the least-damped modes have real phase speeds c_r close to 0.8.

The discrete temporal eigenvalues of the same flow on a compliant layer are given in figure 3 for $\alpha = 0.7$ and $R_{\delta^*} = 1000$. The compliant layer has the following properties: shear wave speed $C_t = 0.35U_\infty$, thickness $h^{(L)} = 1.0$ and a low material damping coefficient. The superscript (L) indicates that the quantity has been specified with respect to a fixed length L (equal to the displacement thickness of the boundary layer at $R_{\delta^*} = 2 \times 10^4$). The corresponding rigid-wall modes are also marked in

https://doi.org/10.1017/S0022112001006206 Published online by Cambridge University Press

		Mode 1		Mode 2	
R_δ	α	c_r	c_i	c_r	c_i
1000	0.1	0.8208	−0.0422	0.7603	−0.1547
1000	0.5	0.8372	−0.0474	0.6450	−0.1878
1000	0.9	0.8287	−0.0442	0.5791	−0.2154
3000	0.1	0.8582	−0.0837	0.0779	−0.3104
3000	0.5	0.7698	−0.0562	0.6284	−0.4316
3000	0.9	0.8433	−0.0773	0.6020	−0.1467

TABLE 1. The two least-damped temporal modes of a turbulent boundary layer on a rigid flat-plate at the Reynolds numbers $R_{\delta^*} = 1000$, 3000 and wavenumbers $\alpha = 0.1$, 0.5, 0.9.

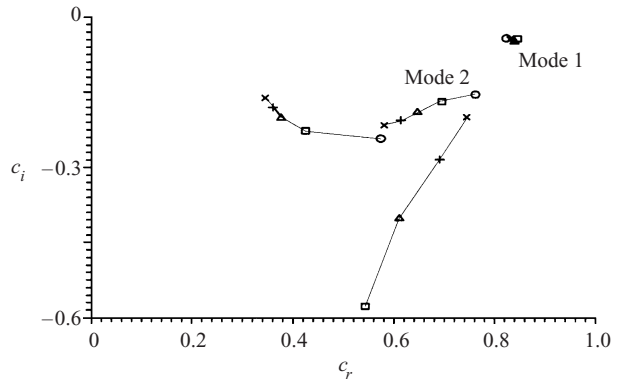


FIGURE 2. The temporal eigenmodes of a turbulent boundary layer on a rigid wall. $R_{\delta^*} = 1000$ and ○, $\alpha = 0.1$; □, $\alpha = 0.3$; △, $\alpha = 0.5$; +, $\alpha = 0.7$; ×, $\alpha = 0.9$.

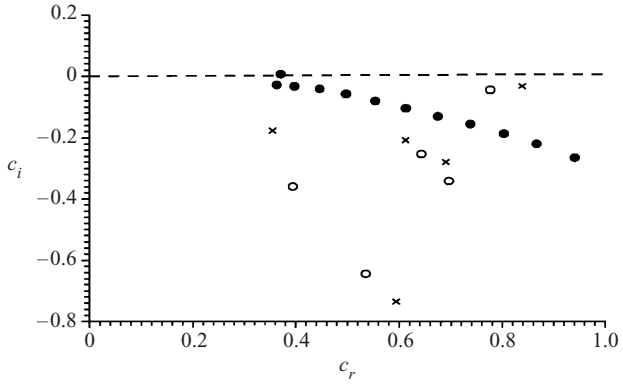


FIGURE 3. The temporal eigenmodes of a turbulent boundary layer on a compliant layer with $h^{(L)} = 1.0$, $C_t = 0.35U_\infty$, $K = 500$ and $d^{(L)} = 0.0049$ at $R_{\delta^*} = 1000$ and $\alpha = 0.7$. Compliant wall: ○, flow modes; ●, wall modes. Rigid wall: ×, flow modes. $M = 60$, $N = 20$.

figure 3 for comparison. The compliant-wall eigenmodes may be divided into two fairly distinct groups. The first group consists (open circular dots) of eigenmodes that are continuously connected to the rigid-wall eigenmodes. They are hence termed the flow modes. They remain damped despite the significant compliance of the layer. The eigenmodes of the second group are marked by full circular dots. All, but one,

https://doi.org/10.1017/S0022112001006206 Published online by Cambridge University Press

are distributed along a fairly well-defined line. These modes are directly allied to the compliance of the layer and are termed the wall modes. One unstable wall mode is discerned in figure 3. Eigenvalues from the present study are found to compare well with those of Hou (1996).

5.2. *Onset of convective and absolute instabilities*

The preceding section shows that the flat-plate turbulent boundary layer may be unstable on a sufficiently compliant surface. We shall now examine the occurrence of instabilities on a compliant layer from the standpoint of the time-asymptotic spatio-temporal theory. Following Kupfer *et al.*, the identification of convective and absolute instabilities is based on the map of the α_i-contours in the complex ω-plane. The α_i-contours for a series of compliant layers with different non-dimensional elastic shear-wave speeds C_t/U_∞ are depicted in figure 4. The displayed contours belong to that of the most unstable or least stable branch (largest ω_i) of ω-eigenmodes. The $\alpha_i = 0$ contours in these figures represent the temporal eigenmodes of course. For a relatively stiff compliant layer (high C_t/U_∞), the $\alpha_i = 0$ contour resides below the real-ω axis, i.e. $\omega_i < 0$ for all temporal modes, and the flow–wall system is temporally stable. As the C_t/U_∞ is reduced, leading to a more compliant layer, the $\alpha_i = 0$ contour rises in the ω-plane, until eventually a part of it goes above the real ω-axis in figure 4(*a*). The latter indicates the onset of unstable temporal modes. The resultant instability is convective in nature; the eigenmodes along the real ω-axis between points *a* and *b* in figure 4(*a*) represent unstable harmonic waves that amplify downstream ($\alpha_i < 0$) of its perturbation source.

A cusp point is formed by the α_i-contours near a value of $\alpha_i \approx -0.13$ in the lower-half ω-plane in figure 4(*a*). The cusp point is created by the coalescence of two α-eigenvalues according to the spatio-temporal theory. As the C_t/U_∞ is further reduced, see figures 4(*b*) and 4(*c*), the flow–wall system becomes convectively unstable to an increasing range of real ω-eigenmodes. Simultaneously, the cusp point advances into the upper-half ω-plane, figure 4(*c*), crossing the real ω-axis at a value of $C_t/U_\infty \approx 0.295$. In the upper-half ω-plane ($\omega_i > 0$) the cusp point denotes an absolute instability mode if causality is satisfied. The causal condition is clearly met since a vertical line drawn upwards from the cusp point intersects the $\alpha_i = 0$ contour only once. Thus, the flat-plate turbulent boundary layer on a compliant wall may be susceptible to both convective and absolute instabilities. Convective instability will generally precede absolute instability because the latter necessarily involves the coalescence of an unstable convective mode with an evanescent mode.

Figure 5 illustrates the coalescence of the α-roots that is responsible for the absolute instability mode in figure 4(*c*). Sen & Arora (1988) and Yeo *et al.* (1996) have found similar coalescence to occur in Blasius boundary layer on soft compliant surfaces. Arising from the coalescence of a Class A and a Class B mode, the coalesced mode is expected to be Class C (Carpenter 1990) and to be mildly stabilized by damping. The coalesced mode indeed exhibited Class C behaviour in the inviscid study of Yeo *et al.* (1999). However, the coalesced modes that we have found here and in Yeo *et al.* (1996) frequently exhibit a Class A energy behaviour. This is especially so with the thicker layers at the lower levels of damping. For thin layers, all three types of energy behaviour may be exhibited by the coalesced mode. It may be pertinent to note that Benjamin's energy classification and equivalent classifications developed by others have been formulated primarily for conservative or nearly conservative systems, and may not be strictly valid for a viscous flow regime. The classification is therefore used here mainly in their phenomenological context to describe the effects of damping.

https://doi.org/10.1017/S0022112001006206 Published online by Cambridge University Press

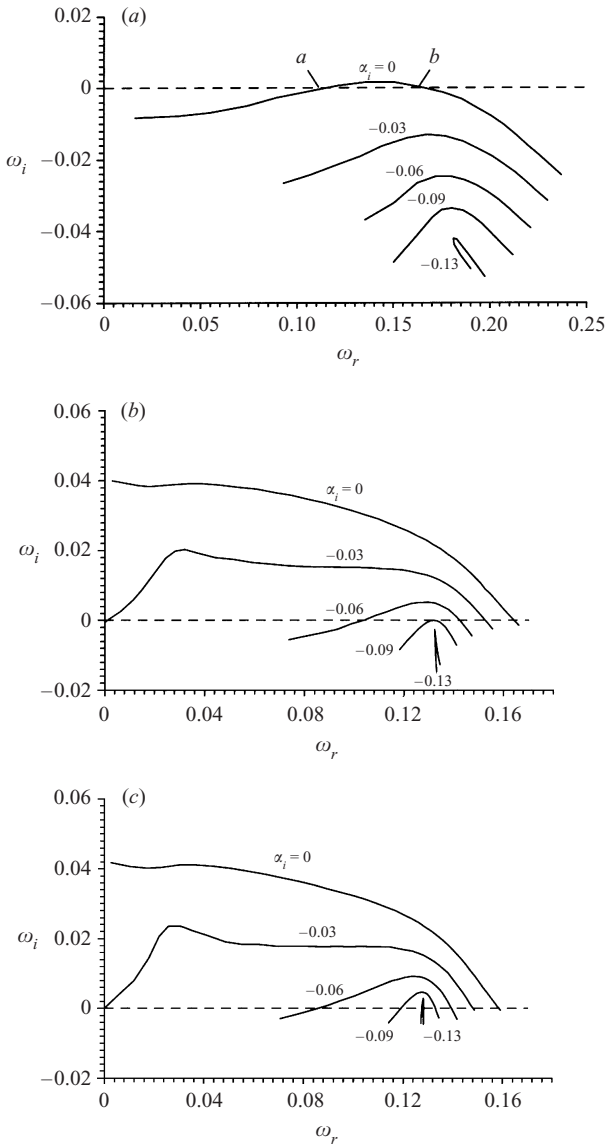


FIGURE 4. The α_i-contours in the complex ω-plane for compliant layers with $h^{(L)} = 0.4$, $K = 500$, $d^{(L)} = 0.02$ and $R_{\delta^*} = 1000$. (*a*) $U_\infty/C_t = 2.200$, (*b*) $U_\infty/C_t = 3.279$, (*c*) $U_\infty/C_t = 3.509$. The onset velocity $U_\infty^{(abs)}/C_t = 3.392$.

5.3. *Effects of other parameters on the onset of convective and absolute instabilities*

In the preceding section, we saw how a reduction in the stiffness of the compliant material had resulted in the successive occurrence of convective and absolute instabilities. The effects of other parameters, such as the layer thickness $h^{(L)}$, the viscoelastic damping coefficient $d^{(L)}$ of the material and the Reynolds number R_{δ^*}, on the onset of the instabilities are examined below.

Figure 6 depicts the onset velocities $(U_\infty/C_t)_{onset}$ of convective and absolute instabilities for two compliant layers, at fixed values of R_{δ^*}, as a function of the thickness $h^{(L)}$. The compliance of the surface generally increases with the thickness of the layer. From the results of the preceding section, one may thus expect the flow to become

https://doi.org/10.1017/S0022112001006206 Published online by Cambridge University Press

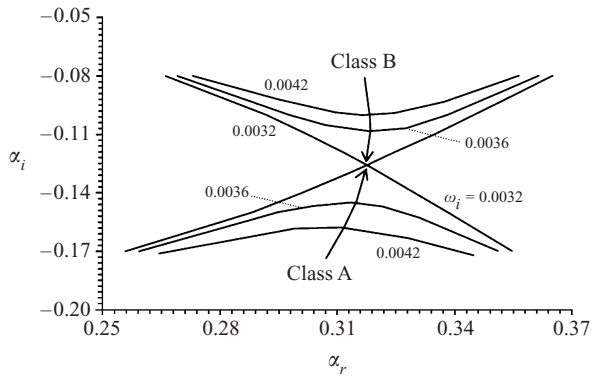


FIGURE 5. Root coalescence or intersection in the α-plane produced by the lowering of the Laplace contour in the ω-plane. The intersection point at $\alpha = (0.3175, -0.1260)$ corresponds to the cusp point in figure 4(*c*).

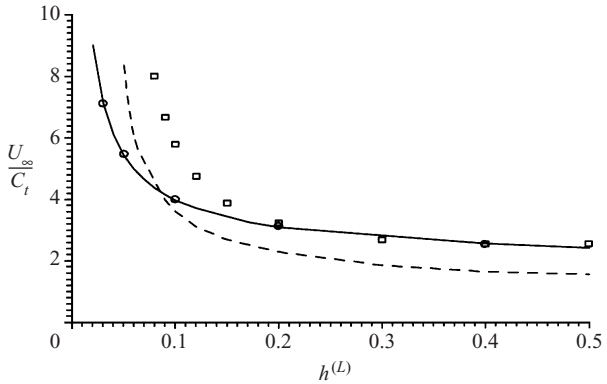


FIGURE 6. Onset velocities for convective and absolute instabilities on compliant layers. Lightly damped layer with $d^{(L)} = 0.0049$ and $R_{\delta^*} = 1100$: - - -, convective modes; q, absolute modes. Highly damped layer with $d^{(L)} = 0.5$, $R_{\delta^*} = 1000$: ——, convective modes; o, absolute modes.

more unstable as $h^{(L)}$ is increased. This is indeed the case, and the effect is manifest in the monotonically decreasing trend of the onset velocity curves; which decrease quite steeply at small $h^{(L)}$ but tend asymptotically to nearly constant values at larger $h^{(L)}$. The $(U_\infty/C_t)_{onset}$ of absolute instability is distinctly higher than the $(U_\infty/C_t)_{onset}$ of convective instability for the lightly damped layer with $d^{(L)} = 0.0049$. This is in line with the expectation that the onset of absolute instability is usually preceded by a convective instability. The situation is changed greatly, however, when the layer is imbued with a much higher level of material damping, $d^{(L)} = 0.5$. For this highly damped layer, the $(U_\infty/C_t)_{onset}$ of the two instabilities are nearly identical over the entire range of $h^{(L)}$.

The effects of material or wall damping on the onset velocities of the two instabilities are more clearly depicted in figure 7 for a thicker layer with $h^{(L)} = 1.0$ at two values of $R_\delta = 1200$ and 2000, and $d^{(L)}$ ranging from 0.005 to 0.5. The $(U_\infty/C_t)_{onset}$ for absolute instability starts at about 3.0 for a nearly elastic layer at $R_{\delta^*} = 1200$. It decreases monotonically with increase in $d^{(L)}$; decreasing fairly rapidly at first and then more gradually, and tending eventually towards a constant value at large $d^{(L)}$. The energy behaviour is thus Class A at lower $d^{(L)}$, and tending to Class C at

https://doi.org/10.1017/S0022112001006206 Published online by Cambridge University Press

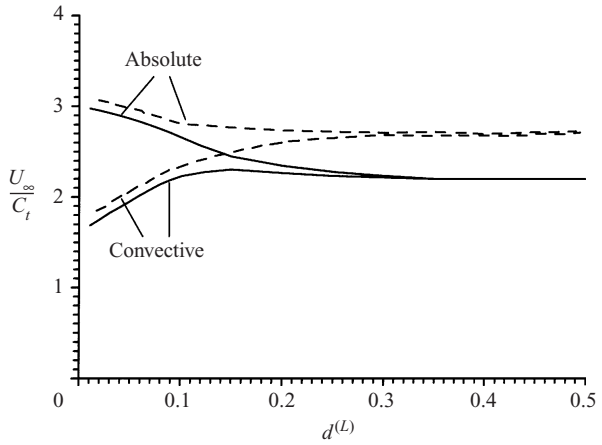


FIGURE 7. Onset velocities for convective and absolute instabilities on compliant layers with thickness $h^{(L)} = 1.0$. ——, $R_{\delta^*} = 1200$; - - -, $R_{\delta^*} = 2000$.

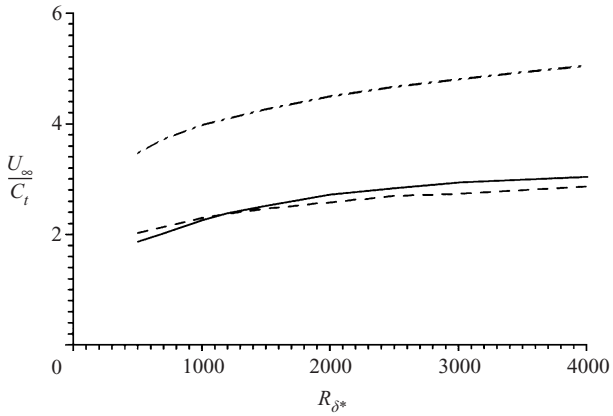


FIGURE 8. Onset velocities for convective and absolute instabilities as functions of Reynolds number R_{δ^*}. $h^{(L)} = 0.1$ and $d^{(L)} = 0.001$: - - -, convective modes. $h^{(L)} = 0.1$ and $d^{(L)} = 0.3$: —·—, convective and absolute modes. $h^{(L)} = 1.0$ and $d^{(L)} = 0.5$: ——, convective and absolute modes.

large $d^{(L)}$. The onset velocity for convective instability, on the other hand, starts off at a significantly lower value of about 1.7, but its value rises fairly rapidly as damping is increased. This is indicative of Class B energy behaviour. It may be supposed that the convective instability of the turbulent boundary layer on a compliant layer is akin to the TWF (a Class B mode) under a laminar boundary layer. The decreasing and increasing $(U_\infty/C_t)_{onset}$ values of the two instabilities cause their onset velocity curves to converge eventually at large values of $d^{(L)}$, with the convective curve lying just below the bounding absolute instability curve at large $d^{(L)}$. The converging curves of convective and absolute instabilities taper forwards as a single curve towards a constant value at very large $d^{(L)}$. The same behavioural trend is repeated at the larger R_{δ^*} of 2000.

The stability of the flow–wall system also changes with the growth of the boundary layer in the stream direction. Figure 8 shows the variation of the $(U_\infty/C_t)_{onset}$ of the instabilities with the Reynolds number R_{δ^*} of the boundary layer. The $(U_\infty/C_t)_{onset}$ for both instabilities are seen to increase with R_{δ^*}, with the rise becoming more gradual

https://doi.org/10.1017/S0022112001006206 Published online by Cambridge University Press

at high R_{δ^*} (computation carried out to $R_{\delta^*} = 10^4$). This means that the instabilities will show a tendency to occur first at the upstream end of a compliant layer and to extend downstream as the compliant layer becomes softer, or as U_∞ is increased. The $(U_\infty/C_t)_{onset}$ curves for the two instabilities are again almost identical for the highly damped layer with $d^{(L)} = 0.5$.

The above suggests that convective instability, with its lower $(U_\infty/C_t)_{onset}$, will be the dominant mode of incipient instability for a mildly damped compliant layer. As wall damping becomes large, the incipient (unstable) convective mode will merge or coalesce with an upstream (of source) evanescent mode to form an absolute mode of instability at a marginally higher onset velocity. The onset velocity difference between the incipient convective instability and the follow-on absolute instability is very small at high damping. Since absolute instability is by far the stronger mode of instability, it will quickly grow to overwhelm any signs of a preceding convective instability. The incipient instability of a zero-pressure-gradient turbulent boundary layer on highly damped viscoelastic layers is hence expected to be absolute in character. This is reminiscent of a similar result for potential flow on compliant surfaces with non-zero damping in Yeo *et al.* (1999).

5.4. *Relation to experimental observations of surface waves*

Highly damped viscoelastic layers were employed in the experiments of Hansen *et al.* (1980) and Gad-el-Hak *et al.* (1984). Gad-el-Hak *et al.* quoted a relaxation time constant of the order of 1 s for their walls, which were materially similar to those of Hansen *et al.* For these highly damped layers, Hansen *et al.* and Gad-el-Hak *et al.* observed a series of large-amplitude spanwise-aligned waves when the flow velocity U_∞ exceeded certain threshold values, that were dependent on the properties of the layers. These spanwise waves traversed the surface of the compliant layers at speeds $c < 0.05U_\infty$. The wave speeds are in fact $< 0.01U_\infty$ at the onset of the waves according to the data given in table 1 of Gad-el-Hak *et al.*, and $< 0.03U_\infty$ for U_∞ exceeding 8–20% of the onset velocity according to table 3 of Hansen *et al.* Their large-amplitude and nearly stationary appearance account for the term static divergence (SD) being applied to these waves, which are also called slow waves here. The SD or slow waves are clearly related to the absolute instability predicted for highly damped layers in the last section. The observations of Gad-el-Hak *et al.* on the birth or initial development of the SD waves are particularly enlightening in this regard. They noted that the appearance of the SD waves was always preceded by a highly transient small-amplitude wavetrain. The evolution of these incipient wavetrains into the SD waves occurred so rapidly that they could not be captured on film. It is plausible that the observed small-amplitude transient waves actually represented the fleeting presence of a precedent convective instability, which was quickly transformed into an absolute instability by mode coalescence at a marginally higher onset velocity, as suggested by the results of figure 7. Gad-el-Hak *et al.* also noted that the SD waves possessed a highly asymmetrical non-sinusoidal waveform with relatively sharp peaks and shallow troughs in between. Absolute instability modes are also likely to have a non-sinusoidal waveform because their wave profiles contain modal contributions from a continuous spectrum. The above discussion shows that the SD waves on highly damped viscoelastic compliant layers are most probably the outcome of an absolute instability.

For nearly elastic compliant layers, Gad-el-Hak (1986) observed instead the occurrence of fairly regular small-amplitude wavetrains. These waves are roughly symmetrical in their profile, if not quite sinusoidal. They travelled at speeds of up to

https://doi.org/10.1017/S0022112001006206 Published online by Cambridge University Press

$0.5U_\infty$ and are termed the fast waves here. They are clearly linked to the convective modes of instability that have been predicted for lightly damped surfaces in the last section.

Nonlinear effects are undoubtedly important in rendering the final form of the observed (post-instability) SD waves. This was demonstrated by Lucey *et al.* (1997) in their numerical simulation of potential flow over highly damped compliant plate panels, where the equilibrated waves exhibit the observed peak–trough feature of the SD waves. Nonlinearity is also evident in the non-sinusoidal waveform of the fast waves. Where it is strong, nonlinearity may also induce modification of the post-instability base flow. There is indeed evidence of this in the enhanced levels of turbulence seen over the SD waves. Given its linear character, it may therefore be expected that not all features of the observed waves will be reproduced faithfully by the present theoretical model. However, the present analyses may yet be effective in capturing the onset conditions for these waves, since the amplitude of the waves would be small in their unstable incipient state. The primary focus of the present paper is hence on predicting the onset conditions for these waves.

5.5. *Onset of SD or slow waves on viscoelastic layers*

Hansen *et al.* (1980) distinguished three types of SD waves in their experiments. As the flow velocity U_∞ was increased, they observed that spanwise surface ridges first began to appear near the leading edge of the compliant layer (Type I SD waves). The waves became more evident and extended further downstream from the leading edge when U_∞ was increased above their initial onset velocity. The Type I waves were followed by Type II and Type III SD waves at a slightly higher U_∞; the latter two waves occurred almost simultaneously and had onset U_∞ that were on the average 17.5% above those of the Type I waves. The Type II SD waves were slightly crescent-shaped ridges that occurred at the side edges of the compliant layers, whereas the Type III SD waves were found in the central region of the compliant surface, seemingly independent of edge conditions. The Type I waves appeared to be triggered by small surface irregularities at the leading edge of the compliant layer. By ensuring a smooth seam there between the layer and the mounting plate in one of their experiments, Hansen *et al.* were able to suppress the waves. With carefully fabricated joints between the compliant layers and the plate, Gad-el-Hak *et al.* had observed only the Type III waves. The sequential appearance of the Type I and Type III waves with increase in the flow velocity U_∞, first near the leading edge and then in the central portion of the compliant surface, respectively, is qualitatively consistent with the theoretical prediction of a slowly increasing $(U_\infty/C_t)_{onset}$ with R_{δ^*} in figure 8.

The onset velocities predicted by the present theoretical model are compared against the experimental results of Hansen *et al.* and Gad-el-Hak *et al.* in figure 9. Since the theoretical onset velocity $(U_\infty/C_t)_{onset}$ is not constant, but increases slowly over the streamwise length of a compliant layer, the experimental onset velocities for the Type I waves are thus compared against the theoretical $(U_\infty/C_t)_{onset}$ at the leading edge (Reynolds number $R^s_{\delta^*}$) of the compliant layer. The Type III wave results of Hansen *et al.* and Gad-el-Hak *et al.*, on the other hand, are compared against the theoretical $(U_\infty/C_t)_{onset}$ at the middle (Reynolds number $R^m_{\delta^*}$) and the downstream end (Reynolds number $R^e_{\delta^*}$) of the compliant layer. The theoretical $(U_\infty/C_t)_{onset}$ at $R^e_{\delta^*}$ represents a situation in which the compliant surface is absolutely unstable at all points, and may be regarded as yielding an approximate condition for the onset of a global absolute instability over the whole compliant surface. Theoretical onset velocity curves at the fixed R_{δ^*} of 500 and 3000, which span the estimated range of

https://doi.org/10.1017/S0022112001006206 Published online by Cambridge University Press

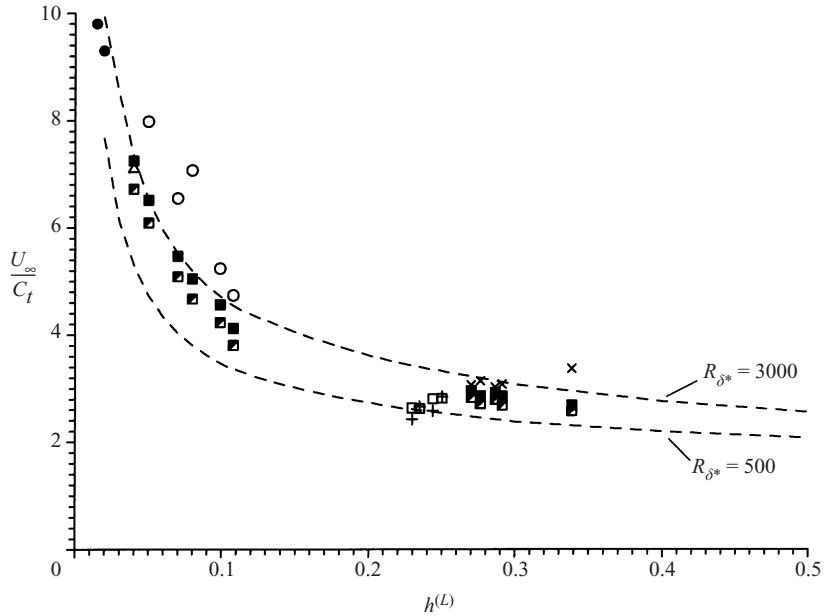


FIGURE 9. Onset velocities for slow or SD waves on damped compliant layers. Experimental results of Hansen *et al.* (1980): +, Type I; ×, Type III. Experimental results of Gad-el-Hak *et al.* (1984): ○, isotropic; △, non-isotropic. Theoretical predictions for compliant layer with $d^{(L)} = 0.5$: q, at start of layer ($R^s_{\delta^*}$); j , at mid-layer ($R^m_{\delta^*}$); r , at end-layer ($R^e_{\delta^*}$). - - -, theoretical onset velocity curves at fixed R_{δ^*}. ●, selected data of Gad-el-Hak *et al.* based on $R^m_{\delta^*} = 2000$.

the experiments, are also depicted in figure 9. All the theoretical results in figure 9 are applicable to viscoelastic layers with a high damping coefficient of $d^{(L)} = 0.5$; which yields relaxation times $\tau_R = d/(\rho C_t^2)$ of 1–2.5 s for the layers tested by Gad-el-Hak *et al.* Hansen *et al.* did not give details about the damping quality of their walls. Their walls were stiffer owing to a higher resin to plasticizer content of about 7% compared to 3% for Gad-el-Hak *et al.* Recalling figure 7, we note that at this high level of damping, any variation in the damping coefficient would only have a relatively small effect on the onset velocity results.

The experimental and theoretical results are in very good agreement for the Type I and Type III waves of Hansen *et al.* The deviations are less than 8% for all except the Type III waves of their experiment 5, for which the predicted value is about 17% lower than the measured value. Nearly half the results show differences of less than 4%. Experiment 5 is the only experiment of their series that used a smaller plate. The principal results of Gad-el-Hak *et al.*, marked by open circles, are derived from their table 1. The agreement of their results with the present theoretical predictions is fairly good in both magnitude and trend, if not quite as sharp as that of Hansen *et al.*'s, Gad-el-Hak *et al.*'s results typically lie above the predicted onset velocities, and span a region where the decrease of onset velocity with thickness $h^{(L)}$ is fairly rapid. The result for a non-isotropic layer (open triangle), also from their table 1, is given in figure 9. For this case, the average thickness of the layer (which was mounted on a streamwise-grooved baseplate) has been used; based on their remark that its onset velocity was approximately the same as that of an isotropic coating of the same average thickness. The non-isotropic layer result is surprisingly in quite good agreement with the present isotropic-layer predictions, lying between the predicted onset velocities at the middle and downstream end of the layer. The onset velocities

https://doi.org/10.1017/S0022112001006206 Published online by Cambridge University Press

for two very thin layers (full circles) are obtained from figure 6 of Gad-el-Hak *et al.* As insufficient details are given for these results in their paper, a midlayer Reynolds number of $R^m_{\delta^*} = 2000$ has been assumed in order to fix the non-dimensional thickness $h^{(L)}$ of the layers. These results are also well placed with respect to the theoretical onset velocity curves. We note that $h^{(L)} \propto R_{\delta^*}$, so that the choice of a different $R^m_{\delta^*}$ within the experimental range would only cause a small horizontal shift of the data points without affecting their overall agreement with the theoretical curves. The present theoretical onset velocity curves also follow closely the overall trend of the experimental results of Hansen *et al.* and Gad-el-Hak *et al.* The modified potential flow model (Yeo *et al.* 1999) merely predicted a constant onset velocity of about 3.0 irrespective of layer thickness.

The present local stability model does not take into account the boundaries of a finite size layer. Instability waves may be inhibited by the constraining effect of a fixed edge. Contrarily, the abrupt change of properties at an edge may be a source of reflected waves that interact with the primary instability wave to give rise to an absolute instability. Such a mechanism will be particularly important for relatively short and lightly damped compliant surfaces, as in Lucey & Carpenter (1992). Surface flaws at an edge may also act as an initiating source for unstable surface waves. The Type III wave results of Hansen *et al.* have agreed very well with the present theoretical predictions when the waves were preceded by the Type I waves. In the absence of the latter, as in experiment 5 of Hansen *et al.* and in Gad-el-Hak *et al.*, the observed $(U_\infty/C_t)_{onset}$ were some 16–20% above the predicted values. This suggests that the Type I waves might have acted as a trigger for the downstream Type III waves. According to Gad-el-Hak (2001, personal communication), the very first appearance of the Type III waves in Gad-el-Hak *et al.* (where Type I waves were absent) was somewhat intermittent and a small excess of flow velocity was generally required to establish a series of sufficiently well-defined waves whose properties could be measured. This may partially explain the higher values of the experimental $(U_\infty/C_t)_{onset}$ compared to the theoretical ones for these cases in figure 9. For Gad-el-Hak *et al.*, the discrete intervals of the test velocities (see their table 1) may also be a contributing factor to the higher recorded $(U_\infty/C_t)_{onset}$.

5.6. *Onset of fast waves on elastic layers*

The onset velocities of the fast waves from Gad-el-Hak (1986) are compared against the theoretical predictions for nearly elastic layers ($d^{(L)} = 0.001$) in figure 10. The experimental results (from figures 3 and 7 of his paper) are compared against the theoretical values at the mid-point and downstream end of the layer. Onset velocity curves at fixed values of R_{δ^*} spanning the experimental range are also depicted to mark the overall theoretical trend. The agreement between the experimental and theoretical onset velocities is fairly good in both magnitude and trend. Indeed, the theoretical results are roughly coincidental with the mean trend of the experimental data points. The experimental data points marked by crosses in figure 10 pertain to cases whose exact U_∞ could not be ascertained from Gad-el-Hak. Their $h^{(L)}$ values have been estimated here by assuming a mid-layer Reynolds number of $R^m_{\delta^*} = 2000$. These data points also fall in quite well with the onset velocity curves; the overall agreement is not affected by the use of a different $R^m_{\delta^*}$.

5.7. *Wavelengths and phase speeds*

Figure 11 gives the predicted wavelengths of the onset SD modes as a function of layer thickness $h^{(L)}$. The small difference between the curves at the R_{δ^*} of 500

https://doi.org/10.1017/S0022112001006206 Published online by Cambridge University Press

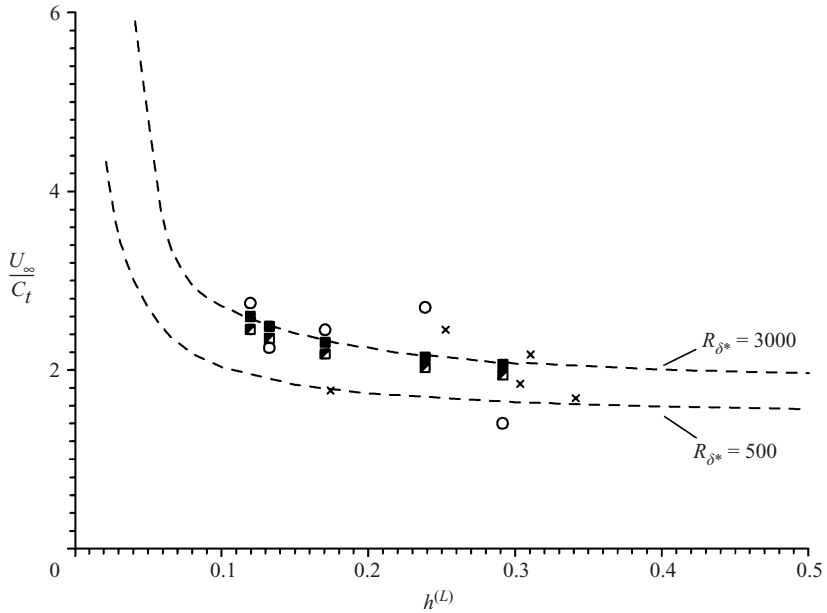


FIGURE 10. Onset velocities for fast waves on elastic compliant layer. ○, Experimental results of Gad-el-Hak (1986). Theoretical predictions for compliant layers with $d^{(L)} = 0.001$: j , at mid-layer ($R^m_{\delta^*}$); r , at end-layer ($R^e_{\delta^*}$). - - -, theoretical onset velocity curves at fixed R_{δ^*}. ×, selected data of Gad-el-Hak based on $R^m_{\delta^*} = 2000$.

and 2500 implies that the wavelength λ increases only very gradually over the length of compliant layers. This is in broad agreement with the experiments. The asymptotic trend of the λ/h curves indicates that λ also scales approximately with the thickness h for the thicker layers. This reinforces the point that the SD is indeed a wall mode, as opposed to a flow mode. The Type I SD waves of Hansen *et al.* have λ (estimated from the figures in their paper) that are slightly larger than the theoretical values. The onset λ/h for the SD waves (Type III) of Gad-el-Hak *et al.* are typically 1.8–2.2 times the theoretical values. Their result for the non-isotropic layer is surprisingly close to the predicted value however. At high $d^{(L)}$, the incipient convective modes that part take in the coalescence leading to absolute instability typically have phase speeds $c_r/U_\infty \approx 0$, see figure 12. This is in agreement with the experiments. This and the convergence of the instabilities suggest that on a highly damped wall, absolute instability and convective instability with $c_r/U_\infty \approx 0$ are practically synonymous.

The λ/h data for the fast waves in figure 11 were deduced from figure 6 of Gad-el-Hak by extrapolation to onset velocities obtained from his figure 7. The experimental λ/h are up to 50% larger than the theoretical values, with good agreement on one data point. The phase speed data of Gad-el-Hak are compared against the theoretical predictions in figure 12. Only values that pertain to the smallest U_∞ for a given layer are selected because these represent conditions that were closest to the onset of the waves. The experimental c_r/U_∞ are generally lower than the theoretical ones based on $d^{(L)}$ of 0.001. Given that nonlinear effects, including the possibility of a modified post-instability base flow, are present in the observed SD and fast waves, some of the above noted disparities between the measured properties of the waves and the present linear stability predictions are not unexpected.

https://doi.org/10.1017/S0022112001006206 Published online by Cambridge University Press

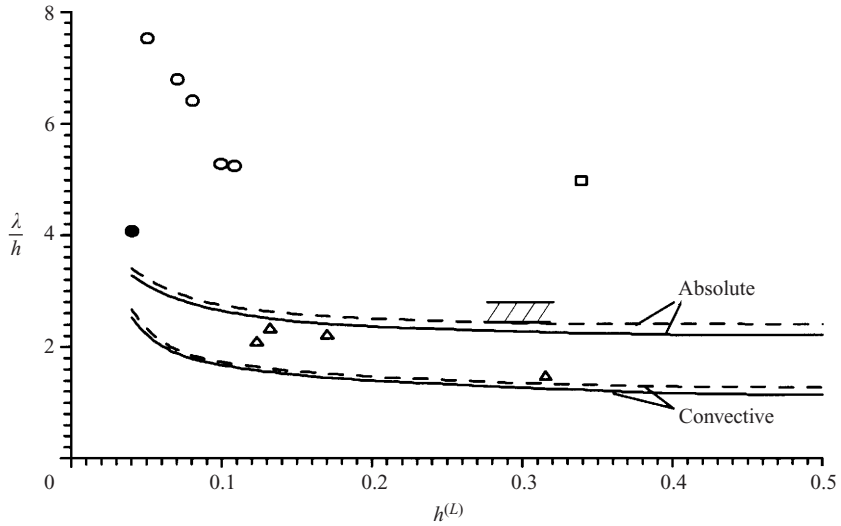


FIGURE 11. Wavelength to thickness ratio. SD or slow waves: Gad-el-Hak *et al.*, ○, isotropic; ●, non-isotropic; ▨ Hansen *et al.*, Type I; q, Type III. Fast waves: △, Gad-el-Hak. Theoretical curves for highly-damped layers $d^{(L)} = 0.5$ (upper set, absolute modes) and nearly-elastic $d^{(L)} = 0.001$ (lower set, convective modes): ——, $R_{\delta^*} = 500$; - - -, $R_{\delta^*} = 2500$.

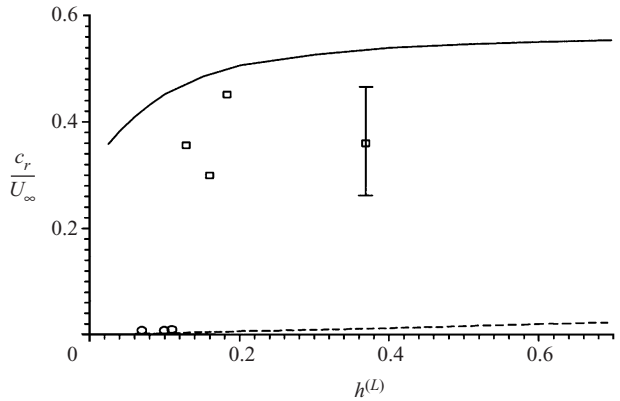


FIGURE 12. Phase speed of slow and fast waves. Fast waves, q, Gad-el-Hak. Slow waves, ○, Gad-el-Hak *et al.* Theoretical curves: ——, fast waves $R_{\delta^*} = 1000$ and $d^{(L)} = 0.001$; - - -, slow waves $R_{\delta^*} = 1000$ and $d^{(L)} = 0.5$.

5.8. *Occurrence of SD waves under laminar flow condition*

All the observed occurrences of SD or slow waves on viscoelastic layers referred to in this paper had taken place under turbulent flow conditions. (Hansen & Hunston (1983) did observe SD-type surface waves under a laminar rotating-disk flow. The latter flow is quite different dynamically from the flow considered in the present study). Gad-el-Hak *et al.* did not find any SD waves when they subjected their test surfaces to laminar flow with U_∞ that were twice the onset values of the waves under turbulent flow conditions. SD waves were found, however, under an artificially induced turbulent wedge in a laminar boundary layer. This demonstrates the readiness of SD waves to form under turbulent flow conditions.

Assuming the SD waves to be associated with the occurrence of absolute instability,

https://doi.org/10.1017/S0022112001006206 Published online by Cambridge University Press

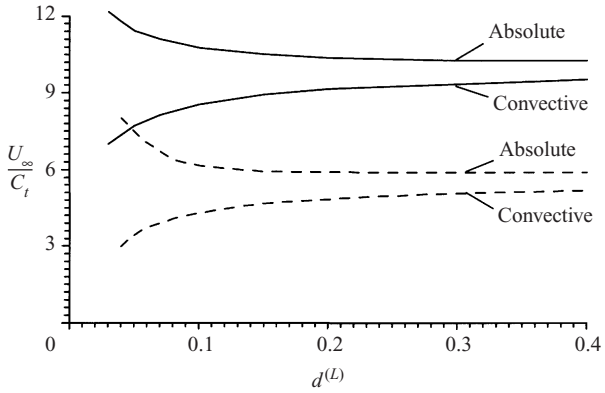


FIGURE 13. Onset velocities for convective and absolute instabilities in laminar (Blasius) boundary layer over compliant layers. - - -, for thickness $h^{(L)} = 5.0$ and $R_{\delta^*} = 3000$; ——, for thickness $h^{(L)} = 0.6$ and $R_{\delta^*} = 2000$.

figure 13 depicts the onset velocities for absolute and convective instabilities in a Blasius boundary layer on two compliant layers as a function of the damping coefficient $d^{(L)}$. The absolute and convective curves for the flow exhibit the same Class A/C and Class B behaviour of the two instabilities as they did under a turbulent boundary layer. However, the absolute and convective curves do not converge as they have done for a turbulent boundary layer in figure 7, and remain distinctly apart even at very high $d^{(L)}$. For the thick layer, $h^{(L)} = 5$, the absolute and convective curves tend to values of 6 and 5, respectively, at large $d^{(L)}$. The thinner layer, $h^{(L)} = 0.6$, has a large onset velocity for absolute instability of about 10 at large $d^{(L)}$, and the onset velocity rises very rapidly when $h^{(L)}$ is reduced below 0.5. The compliant layers tested by Gad-el-Hak *et al.* are much thinner than those in figure 13, and may be expected to have onset velocities in excess of those used in the experiments. This may explain why Gad-el-Hak *et al.* failed to find any SD waves under a laminar boundary layer. It is also possible SD waves may never form under a laminar boundary layer, even on a thick compliant layer such as the $h^{(L)} = 5$ in figure 13, for another reason. With a distinctly lower onset velocity, convective instability may well dominate the flow and cause it to undergo transition to a turbulent state before laminar absolute instability has a chance to set in. In this case, we will merely witness a transition to turbulence and an ensuing SD instability, under turbulent flow condition, that completely bypasses laminar absolute instability.

5.9. *Three-dimensional wave modes*

A preliminary study of three-dimensional wave modes was also carried out as part of the present study to appraise the significance of three-dimensional effects. The three-dimensional wave problem was cast in its equivalent two-dimensional form, following Yeo (1992). Results for spanwise-periodic modes (real spanwise wavenumber β) were obtained. The causality requirement for real-β modes is identical to that for two-dimensional ($\beta = 0$) modes. For general three-dimensional modes (complex α and β), simultaneous deformation of the Fourier contours in the two wavenumber planes would be required to reveal the causal pinch points (Bers 1983). Some complex-β coalescence modes that are contiguous with real-β modes were obtained by a continuation procedure. These had all turned out, however, to be non-causal, suggesting the possibility that there may be no absolute instability with spanwise growth. (This

https://doi.org/10.1017/S0022112001006206 Published online by Cambridge University Press

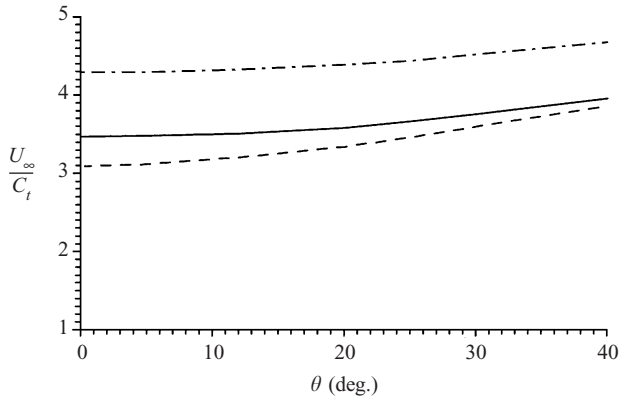


FIGURE 14. The onset velocity of convective and absolute three-dimensional modes in a turbulent boundary layer. Compliant layer with $h^{(L)} = 0.4$, $d^{(L)} = 0.049$ and $R_\delta = 1000$: - - -, convective modes; —·—, absolute modes. Compliant layer with $h^{(L)} = 0.2$, $d^{(L)} = 0.5$ and $R_{\delta^*} = 2000$: ——, convective and absolute modes.

does not rule out the possible existence of discrete complex (α, β) absolute instability modes.)

Figure 14 shows the onset flow velocities of convective and absolute instabilities for two compliant layers as a function of the oblique wave angle $\theta = \tan^{-1}(\beta/\alpha_r)$. Distinct onset convective and absolute instability curves are shown for the more lightly damped layer ($d^{(L)} = 0.049$), whereas the highly damped layer ($d^{(L)} = 0.5$) only has a single merged curve, similar to the two-dimensional case. For all the cases considered, the two-dimensional modes clearly have the lowest onset velocities and are hence the unstable modes (Zhao 1999). This agrees well with the observed two-dimensional spanwise character of the incipient SD waves. Gad-el-Hak (1986) did not comment on the two-dimensionality of the fast waves, but the above result indicates that this is likely to be the case. The two-dimensional character of these instabilities is also consistent with their being wall modes (see § 5.1 and Yeo 1992).

5.10. *Turbulent flow–compliant wall interactions*

All instabilities are expected to influence changes to the base flow. The instabilities we have studied here produce well-defined waves on compliant surfaces that are related to the outer scales of the boundary layer. In the aftermath of instability, a modified turbulent flow may be established. The new turbulent flow may experience a higher or a lower drag than the original base flow. For laminar boundary layer on a flat-plate, instability typically leads to drag increase owing to an ensuing laminar–turbulent transition. Surface drag is increased by SD waves acting as roughness elements under a turbulent boundary layer, but nothing is known for sure about the fast waves. The recent experiments of Choi *et al.* (1997) found compliant surfaces under a turbulent boundary layer to yield drag reductions of up to 7%. The reduction in drag is associated with an outward shift of the logarithmic region of the boundary layer, a phenomenon already noted in earlier experiments by Lee, Fisher & Schwarz (1993). The change in boundary-layer characteristics was attributed to an interaction between the fine-scale near-wall structures of the turbulent flow and the compliant surface. As explained in § 2.1, the present model is not able to treat such fine-scale events. Bushnell, Hefner & Ash (1977) had surmised that near-wall flow–wall interaction might interfere with the bursting events of turbulence, with beneficial effect on the

https://doi.org/10.1017/S0022112001006206 Published online by Cambridge University Press

drag. To date, progress in this direction has been hampered by the lack of a suitable theoretical model to describe the fine-scale interaction between near-wall turbulence and the boundary.

6. Concluding summary

A linear stability model of incompressible two-dimensional turbulent boundary layer over viscoelastic compliant layers is developed in the present study. The principal Reynolds stress and its perturbation are modelled by a mixing-length eddy-viscosity mechanism. The instabilities are classified as convective or absolute in accordance with their asymptotic spatio-temporal characteristics. This division corresponds one for one with the experimental observations of the fast waves and slow/SD waves on elastic and highly damped viscoelastic compliant surfaces, respectively.

The instability of the turbulent boundary layer is derived from the excitation of wall modes. The instabilities are hence amplified by an increase in wall compliance, which may arise from a reduction in the stiffness of the wall material or an increase in the thickness of the compliant layer. Convective instability usually precedes absolute instability.

Compliant surfaces with low damping are susceptible to convective instability, whose onset velocity rises with an increase in wall damping in the typical Class B fashion. The onset velocity for absolute instability, on the other hand, decreases with an increase in damping, so that at high levels of damping, the two instabilities converge as one. Compliant surfaces with high damping are therefore dominated by an absolute instability, whose spatio-temporal character correlates well with the nearly stationary appearance and the strong growth of the observed SD waves. This convergence of onset velocities does not hold for the Blasius (laminar) boundary layer. Because of the distinctly lower onset velocity for convective instability in a laminar boundary layer, absolute instability of the flow may be bypassed by the transition of the flow to a turbulent state owing to the precedent convective instability.

The theoretical model predicts onset velocities that are in fairly good agreement with the experiments for both fast and slow/SD waves. A preliminary study of three-dimensional waves suggests that the two-dimensional modes are indeed the most unstable. This is in agreement with the observed spanwise-aligned appearance of the incipient SD waves.

REFERENCES

Benjamin, T. B. 1960 Effects of a flexible boundary on hydrodynamic stability. *J. Fluid Mech.* **6**, 161.

Benjamin, T. B. 1963 The three-fold classification of unstable disturbances in flexible surfaces bounding inviscid flows. *J. Fluid Mech.* **16**, 436.

Bers, A. 1983 *Handbook of Plasma Physics*, Chap. 3. North-Holland.

Boggs, F. W. & Hahn, E. R. 1962 Performance of compliant skins in contact with high velocity flow in water. In *Proc. 7th Joint-Army-Navy-Air Force Conf. on Elastomer Research and Development*. San Francisco, USA Office of Naval Research, vol. 2, p. 443.

Briggs, R. J. 1964 *Electron-Stream Interaction with Plasmas*. MIT Press.

Bushnell, D. M., Hefner, J. N. & Ash, R. I. 1977 Effect of compliant wall motion on turbulent boundary layers. *Phys. Fluids* **20**, S31.

Carpenter, P. W. 1990 Status of transition delay using compliant walls. *Viscous Drag Reduction in Boundary Layers* (ed. D. M. Bushnell & J. N. Hefner), p. 79. AIAA.

Carpenter, P. W. & Garrad, A. D. 1985 The hydrodynamic stability of flow over Kramer-type compliant surfaces. Part 1. Tollmien–Schlichting instabilities. *J. Fluid Mech.* **155**, 465.

https://doi.org/10.1017/S0022112001006206 Published online by Cambridge University Press

Cebeci, T. & Bradshaw, P. 1977 *Momentum Transfer in Boundary Layer*. Hemisphere.

Choi, K. S., Yang, X., Clayton, B. R., Glover, E. J., Atlar, M., Semenov, B. N. & Kulik, V. M. 1997 Turbulent drag reduction using compliant surfaces. *Proc. R. Soc. Lond.* A **453**, 2229.

Coles, D. 1956 The law of the wake in the turbulent boundary layer. *J. Fluid Mech.* **1**, 191.

Crighton, D. G. & Oswell, J. E. 1991 Fluid loading with mean flow. I. Response of an elastic plate to localized excitation. *Phil. Trans. R. Soc. Lond.* A **335**, 557.

Duncan, J. H., Waxman, A. M. & Tulin, M. P. 1985 The dynamics of waves at the interface between a viscoelastic coating and a fluid flow. *J. Fluid Mech.* **158**, 177.

Evrensel, A. & Kalnins, A. 1988 Response of a compliant slab to viscous incompressible fluid flow. *Trans. ASME* E: *J. Appl. Mech.* **55**, 660.

Ffowcs Williams, J. E. 1964 Reynolds stress near a flexible surface responding to unsteady air flow. *Bolt Beranek and Newman Inc., Rep.* 1138, 1.

Gad-el-Hak, M. 1986 The response of elastic and viscoelastic surfaces to a turbulent boundary. *Trans. ASME* E: *J. Appl. Mech.* **53**, 206.

Gad-el-Hak, M., Blackwelder, R. F. & Riley, J. J. 1984 On the interaction of compliant coatings with boundary-layer flow. *J. Fluid Mech.* **140**, 257.

Hansen, R. J. & Hunston, D. L. 1983 Fluid-property effects on flow-generated waves on a compliant surface. *J. Fluid Mech.* **133**, 161.

Hansen, R. J., Hunston, D. L., Ni, C. C. & Reischman, M. M. 1980 An experimental study of flow-generated waves on a flexible surface. *J. Sound Vib.* **68**, 317.

Hinze, J. O. 1975 *Turbulence*, chap. 6, 2nd Edn. McGraw-Hill.

Hou, J. T. 1996 The stability analysis of turbulent mean flow over a compliant wall. MEng. thesis, National University of Singapore, Singapore.

Huerre, P. & Monkewitz, P. A. 1990 Local and global instabilities in spatially developing flows. *Annu. Rev. Fluid Mech.* **22**, 473.

Hussain, A. K. M. F. & Reynolds, W. C. 1970 The mechanics of perturbation wave in turbulent shear flow. Dept Mech. Engng Rep. Stanford University, FM6.

Kupfer, K., Bers, A. & Ram, A. K. 1987 The cusp map in the complex-frequency plane for absolute instabilities. *Phys. Fluids* **30**, 3075.

Landahl, M. T. 1962 On the stability of laminar incompressible boundary layer over a flexible surface. *J. Fluid Mech.* **13**, 609.

Landahl, M. T. 1967 A wave-guide model for turbulent shear flow. *J. Fluid Mech.* **29**, 441.

Lee, T., Fisher, M. & Schwarz, W. H. 1993 Investigation of stable interaction of a passive compliant surface with a turbulent boundary layer. *J. Fluid Mech.* **257**, 373.

Lucey, A. D., Cafolla, G. J., Carpenter, P. W. & Yang, M. 1997 The nonlinear hydroelastic behaviour of flexible walls. *J. Fluids Struct.* **11**, 717.

Lucey, A. D. & Carpenter, P. W. 1992 A numerical simulation of the interaction of a compliant wall and inviscid flow. *J. Fluid Mech.* **234**, 121.

Markus, W. V. R. 1956 Outline of a theory of turbulent shear flow. *J. Fluid Mech.* **1**, 521.

Pope, S. B. 1975 A more general effective-viscosity hypothesis. *J. Fluid Mech.* **72**, 331.

Reynolds, W. C. & Hussain, A. K. M. F. 1972 The mechanics of an organized wave in turbulent shear flow. Part 3. Theoretical models and comparisons with experiments. *J. Fluid Mech.* **54**, 263.

Semenov, B. N. 1971 Interaction of an elastic boundary with the viscous sublayer of a turbulent layer. *NASA TT F-14*, 391.

Sen, P. K. & Arora, D. S. 1988 On the stability of laminar boundary-layer flow over a flat plate with compliant surface. *J. Fluid Mech.* **197**, 201.

Sen, P. K. & Veeravalli, S.V. 1998 On the behaviour of organized disturbances in a turbulent boundary layer. *Sādhanā* **23**(2), 167.

Speziale, C. G. 1991 Analytical methods for development of Reynolds-stress closures in turbulence. *Annu. Rev. Fluid Mech.* **23**, 379.

Tennekes, H. & Lumley, J. L. 1972 *A First Course in Turbulence*. MIT Press.

White, F. M. 1991 *Viscous Fluid Flow*. McGraw-Hill.

Yeo, K. S. 1988 The stability of boundary-layer flow over single- and multi-layer viscoelastic walls. *J. Fluid Mech.* **196**, 359.

https://doi.org/10.1017/S0022112001006206 Published online by Cambridge University Press

Yeo, K. S. 1992 The three-dimensional stability of boundary-layer flow over compliant walls. *J. Fluid Mech.* **238**, 537.

Yeo, K. S. & Dowling, A. P. 1987 The stability of inviscid flow over passive compliant wall. *J. Fluid Mech.* **183**, 265.

Yeo, K. S., Khoo, B. C. & Zhao, H. Z. 1996 The absolute instability of boundary-layer flow over viscoelastic wall. *Theor. Comput. Fluid Dyn.* **8**, 237.

Yeo, K. S., Khoo, B. C. & Zhao, H. Z. 1999 The convective and absolute instability of fluid flow over viscoelastic compliant layers. *J. Sound Vib.* **223**, 379.

Zhao, H. Z. 1999 The absolute and convective instability of boundary-layer flows over compliant walls. PhD thesis, National University of Singapore, Singapore.

Zimmermann, G. 1974 Interaction between a turbulent boundary layer and a flexible wall. *Rep. 10a*, Max-Planck-Institut für Strömungsforschung Göttingen, Germany.

https://doi.org/10.1017/S0022112001006206 Published online by Cambridge University Press